Mon. Not. R. Astron. Soc. **000**, – (2018) Printed 30 July 2018 (MN LaTeX style file v2.2)

Measuring Linear and Non-linear Galaxy Bias Using Counts-in-Cells in the Dark Energy Survey Science Verification Data

A. I. Salvador[1⋆], F. J. Sánchez[2,3]†, A. Pagul[4,5], J. García-Bellido[1], E. Sanchez[3], A. Pujol[6,7], J. Frieman[8,5], E. Gaztanaga[9,10], A. J. Ross[11], I. Sevilla-Noarbe[3], T. M. C. Abbott[12], S. Allam[8], J. Annis[8], S. Avila[13], E. Bertin[14,15], D. Brooks[16], D. L. Burke[17,18], A. Carnero Rosell[19,20], M. Carrasco Kind[21,22], J. Carretero[23], F. J. Castander[9,10], C. E. Cunha[17], J. De Vicente[3], H. T. Diehl[8], P. Doel[16], A. E. Evrard[24,25], P. Fosalba[9,10], D. Gruen[17,18], R. A. Gruendl[21,22], J. Gschwend[19,20], G. Gutierrez[8], W. G. Hartley[16,26], D. L. Hollowood[27], D. J. James[28], K. Kuehn[29], N. Kuropatkin[8], O. Lahav[16], M. Lima[30,19], M. March[31], J. L. Marshall[32], F. Menanteau[21,22], R. Miquel[33,23], A. K. Romer[34], A. Roodman[17,18], V. Scarpine[8], R. Schindler[18], M. Smith[35], M. Soares-Santos[36], F. Sobreira[37,19], E. Suchyta[38], M. E. C. Swanson[22], G. Tarle[25], D. Thomas[13], V. Vikram[39], A. R. Walker[12]

(DES Collaboration)

Affiliations listed at the end of this document

30 July 2018

ABSTRACT

Non-linear bias measurements require a great level of control of potential systematic effects in galaxy redshift surveys. Our goal is to demonstrate the viability of using Counts-in-Cells (CiC), a statistical measure of the galaxy distribution, as a competitive method to determine linear and higher-order galaxy bias and assess clustering systematics. We measure the galaxy bias by comparing the first four moments of the galaxy density distribution with those of the dark matter distribution. We use data from the MICE simulation to evaluate the performance of this method, and subsequently perform measurements on the public Science Verification (SV) data from the Dark Energy Survey (DES). We find that the linear bias obtained with CiC is consistent with measurements of the bias performed using galaxy-galaxy clustering, galaxy-galaxy lensing, CMB lensing, and shear+clustering measurements. Furthermore, we compute the projected (2D) non-linear bias using the expansion $\delta_g = \sum_{k=0}^{3} (b_k/k!)\delta^k$, finding a non-zero value for b_2 at the 3σ level. We also check a non-local bias model and show that the linear bias measurements are robust to the addition of new parameters. We compare our 2D results to the 3D prediction and find compatibility in the large scale regime (> 30 Mpc h^{-1}).

Key words: data analysis – cosmological parameters – dark energy – large-scale structure of the universe – bias – clustering systematics

1 INTRODUCTION

In recent years, photometric redshift galaxy surveys such as the Sloan Digital Sky Survey (SDSS) (Kollmeier et al. 2017), the Dark Energy Survey (DES) (Dark Energy Survey Collaboration et al. 2016), and the future Large Synoptic Survey Telescope (LSST) (Ivezić et al. 2008) and Euclid (Amiaux et al. 2012), have arisen as powerful probes of the Large Scale Structure (LSS) of the universe and of dark energy. The main advantage of these surveys is their ability to retrieve information from a vast number of objects, yielding unprecedented statistics for different observables in the study of LSS. Their biggest drawback is the lack of line-of-

⋆ Email:ana.salvador@uam.es
† Email:francs1@uci.edu

sight precision and the systematic effects associated with it. Thus, well constrained systematic effects and robust observables are required in order to maximize the performance of such surveys. In this context, simple observables such as the galaxy number counts serve an important role in proving the robustness of a survey. In particular, the galaxy Counts-in-Cells (CiC), a method that consists of counting the number of galaxies in a given three-dimensional or angular aperture, has been shown to provide valuable information about the LSS (Peebles 1980; Gaztañaga 1994; Bernardeau 1994) and gives an estimate of how different systematic effects can affect measurements. CiC can provide insights to higher-order statistical moments of the galaxy counts without requiring the computation resources of other methods (Gil-Marín et al. 2015), such as the three- or four-point correlation functions.

Understanding the relation between galaxies and matter (galaxy bias) is essential for the measurements of cosmological parameters (Gaztanaga et al. 2011). The uncertainties in this relation strongly increase the errors in the dark energy equation of state or gravitational growth index (Eriksen & Gaztanaga 2015). Thus, having a wide variety of complementary methods to determine galaxy biasing can help break degeneracies and improve the overall sensitivity for a given galaxy survey.

In this paper we present a method to extract information from the galaxy CiC. Using this method, we measure the projected (angular) galaxy bias (linear and non-linear) in both simulations and observational data from DES, we compare the measured and predicted linear and non-linear bias, and we test for the presence of systematic effects. This dataset is ideal for this study since it has been already used for CiC in Clerkin et al. (2016) where the authors found that the galaxy density distribution and the weak lensing convergence (κ_{WL}) are well described by a lognormal distribution. The main difference between our study and Clerkin et al. (2016) is that our main goal is to provide a measurement of the galaxy bias, whereas Clerkin et al. (2016) study convergence maps.

The authors in Gruen et al. (2017) also perform CiC in DES data. Combining gravitational lensing information and CiC, they measure the galaxy density probability distribution function (PDF) and obtain cosmological constraints using the `redMaGiC` selected galaxies (Rozo et al. 2016) in DES Y1A1 photometric data (Drlica-Wagner et al. 2018). In our case we measure the moments of the galaxy density contrast PDF and compare them to the matter density contrast PDF from simulations (with the same redshift distributions) to study different biasing models, in a different galaxy sample (DES-SV).

Throughout the paper, we assume a fiducial flat ΛCDM+ν (one massive neutrino) cosmological model based on Planck 2013 + WMAP polarization + ACT/SPT + BAO, with parameters (Ade et al. 2014) $\omega_b = 0.0222$, $\omega_c = 0.119$, $\omega_\nu = 0.00064$, $h = 0.678$, $\tau = 0.0952$, $n_s = 0.961$ and $A_s = 2.21 \times 10^{-9}$ at a pivot scale $\bar{k} = 0.05\mathrm{Mpc}^{-1}$ (yielding $\sigma_8 = 0.829$ at $z = 0$), where $h \equiv H_0/100\mathrm{km\ s}^{-1}\mathrm{Mpc}^{-1}$ and $\omega_i \equiv \Omega_i h^2$ for each species i.

The paper is organized as follows: in Section 2, we present the data sample used for our analysis. First, we present the simulations used to test and validate the method and afterwards, the dataset in which we perform our measurements. In Section 3, we present the CiC theoretical framework and detail our method to obtain the linear and non-linear bias. Section 4 and 5 present the CiC moments and bias calculations for the MICE simulation and DES-SV dataset, respectively. In Section 6, we study the systematic uncertainties in our method. Finally, in Section 7, we include some concluding remarks about this work.

2 DATA SAMPLE

2.1 Simulations

In order to test and validate the methodology presented in this paper, we use the MICE simulation (Fosalba et al. 2008; Crocce et al. 2010). MICE is an N-body simulation with cosmological parameters following a flat ΛCDM model with $\Omega_m = 0.25$, $\Omega_\Lambda = 0.75$, $\Omega_b = 0.044$, $n_s = 0.95$, and $\sigma_8 = 0.8$. The simulation covers an octant of the sky, with redshift z, between 0 and 1.4 and contains 55 million galaxies in the lightcone. The simulation has a comoving size $L_{box} = 3072h^{-1}$Mpc and more than $8 \cdot 10^9$ particles (Crocce et al. 2015). The galaxies in the MICE simulation are selected following the procedure in Crocce et al. (2016), imposing the threshold $i_{evol} < 22.5$. The MICE simulation has been extensively studied in the literature (Sánchez et al. 2011; Crocce et al. 2016; Hoffmann et al. 2015; Pujol et al. 2017; Garcia-Fernandez et al. 2018), including measurements of the higher-order moments in the dark matter field (Fosalba et al. 2008), providing an ideal validation sample.

2.2 The DES SV Benchmark Data Sample

In this paper we perform measurements of the density contrast distribution and its moments on the DES Science Verification (SV) photometric sample [1] (Figure 1). The DES Science Verification observations were taken using DECam on the Blanco 4m Telescope near La Serena, Chile, covering over 250 deg^2 at close to DES nominal depth. From this sample we make selection cuts in order to recover the LSS Benchmark sample (Crocce et al. 2016). By doing this we minimize the possible two-point systematic effects and we ensure completeness. We focus on the SPT-E field, since it is the largest contiguous field and the best analyzed, with $60° < \mathrm{RA} < 95°$, and $-60° < \mathrm{Dec} < -40°$ considering only objects with $18 < i < 22.5$ where i is `MAG_AUTO` as measured by `SExtractor` (Bertin & Arnouts 1996) in the i-band. The star-galaxy separation is performed by selecting objects such that `WAVG_SPREAD_MODEL` > 0.003. The total area considered for our study is then 116.2 deg^2 with approximately 2.3 million objects and a number density $n_g = 5.6$ arcmin^{-2}. Several photo-z estimates are available for these data. We will focus on the TPZ catalog (Carrasco Kind & Brunner 2013) and use the same 5 redshift bins used in Crocce et al. (2016) with the redshift distribution depicted in Figure 2.

Several measurements of the linear bias have been performed using this field (Crocce et al. 2016; Giannantonio et al. 2016; Prat et al. 2018), making it ideal for this study.

[1] This sample is available at `https://des.ncsa.illinois.edu/releases/sva1`

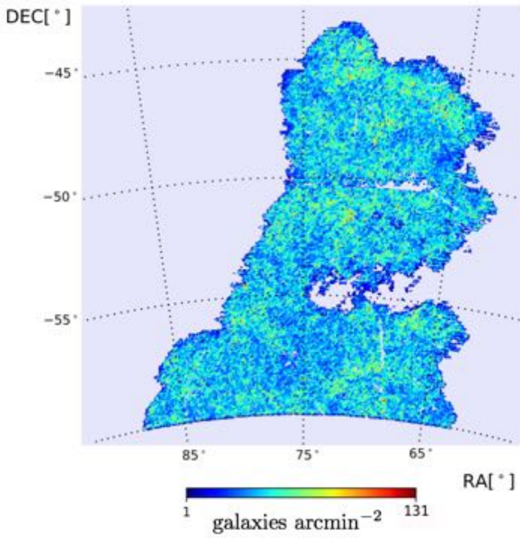

Figure 1. Footprint of the DES SV benchmark sample (Crocce et al. 2016). We use approximately 2.3 million objects contained within this area for our studies.

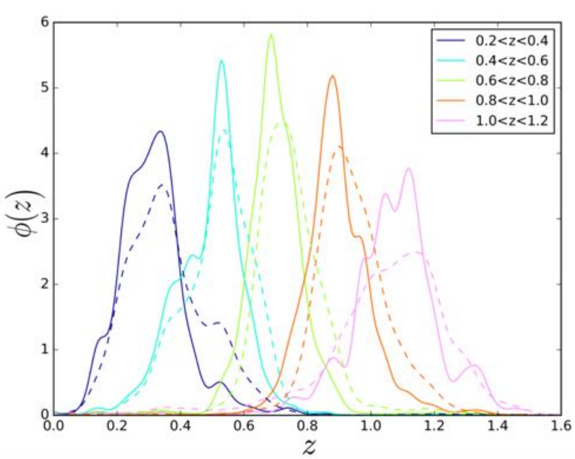

Figure 2. Redshift distribution of the galaxies in each photometric redshift bin using TPZ (solid line) and BPZ (dashed line) in DES-SV benchmark data from Crocce et al. (2016).

3 THEORETICAL FRAMEWORK AND METHODOLOGY

3.1 Counts-in-cells

Counts-in-Cells (Peebles 1980) is a method used to analyze the LSS and is based on dividing a galaxy survey into cells of equal volume ($V_{\rm pix}$) and counting the number of galaxies in each cell, ($N_{\rm gal}$). It is particularly useful to work with the density contrast, δ_i in each pixel, i, defined as:

$$\delta_i \equiv \frac{\rho_i}{\langle\rho\rangle} - 1 \tag{1}$$

where $\rho_i \equiv \frac{N_{i,\rm gal}}{V_{i,\rm pix}}$ is galaxy density in the pixel and $\langle\rho\rangle$ is the mean density. Given this definition, it follows that $\langle\delta\rangle = 0$. The information that we are interested in is encoded in the statistical moments of the density contrast distribution:

$$m_{j>1} \equiv \langle\delta^j\rangle = \frac{1}{N_{\rm pix}} \sum_i (\delta_i - \langle\delta\rangle)^j \tag{2}$$

where $N_{\rm pix}$ is the number of pixels inside the survey.
The connected moments of the smoothed density field are the average of the J-point correlation functions in a cell of volume V (Gaztañaga 1994):

$$\begin{aligned} &\bar{\xi}_J(V) \equiv \langle\delta^J\rangle \equiv \\ &\equiv \frac{1}{V^J}\int ... \int d^3r_1 ... d^3r_J \xi_J(r_1, ..., r_J) W(r_1) ... W(r_J) \end{aligned} \tag{3}$$

with $W(r_J)$ window functions. Averaging over spheres of radius R, the rescaled connected moments S_J can be defined as:

$$S_J(R) \equiv \frac{\bar{\xi}_J(R)}{[\bar{\xi}_2(R)]^{J-1}}, \quad J > 2 \tag{4}$$

With $S_2(R) = \bar{\xi}_2(R)$. In practice, what we measure are the central moments m_J of the angular counts. But because we ultimately want to obtain the connected moments, we need to subtract the lower order contributions. Due to the discreteness of CiC statistics, we also have to take into account the shot noise $\delta_{\rm SN}$. We assume that the galaxies and the matter density field follow a Poissonian distribution and compute the shot-noise corrections and connected moments that can be found in Appendix A. These definitions can easily be generalized for angular aperture cells. This kind of cell is more suitable for photometric redshift galaxy surveys like DES given the relative lack of precision in the determination of distances along the line-of-sight compared to spectroscopic surveys. For the area-averaged angular correlations $\overline{w}_J(\theta)$:

$$S_J \equiv \frac{\overline{w}_J(\theta)}{[\overline{w}_2(\theta)]^{J-1}}, \quad J > 2 \tag{5}$$

In the angular case the moments are the average of the J-point angular correlation functions in a cell of area A (Gaztañaga 1994):

$$\overline{w}_J(\theta) = \frac{1}{A^J}\int_A dA_1 ... dA_J w_J(\theta_1, ..., \theta_J) \tag{6}$$

To obtain the second order moment, $S_2(\theta)$, we can integrate the angular two point correlation function $w_2(\theta)$:

$$w_2(\theta) = \int dz_1 \int dz_2 \; \phi(z_1)\phi(z_2)\xi(r(z_1, z_2)) \tag{7}$$

where $\theta = \arccos(\overline{\Omega}_1 \cdot \overline{\Omega}_2)$ is the cell aperture, $\phi(z)$ is the redshift distribution of the sample, and $\xi(r(z_1, z_2))$ the correlation function. Integrating over one pixel:

$$\overline{w}_2(\theta) = \frac{1}{A^2_{\rm pix}}\int w_2(\theta) d\Omega_1 d\Omega_2 \tag{8}$$

In most previous studies, the cells considered were spheres with radii of varying apertures (Peebles (1980), Bernardeau (1994)). We perform our measurements of the projected (angular) density contrast by dividing the celestial sphere into `HEALpix` pixels (Górski et al. 2005). For our study we vary the `HEALPix` parameter N_{side} from 32 to 4096 (*i.e.* apertures ranging from 1.83° to 0.014°). The angular aperture, θ, is estimated as the square root of the pixel area. According to equation (3) there is a dependence on the boundaries of the

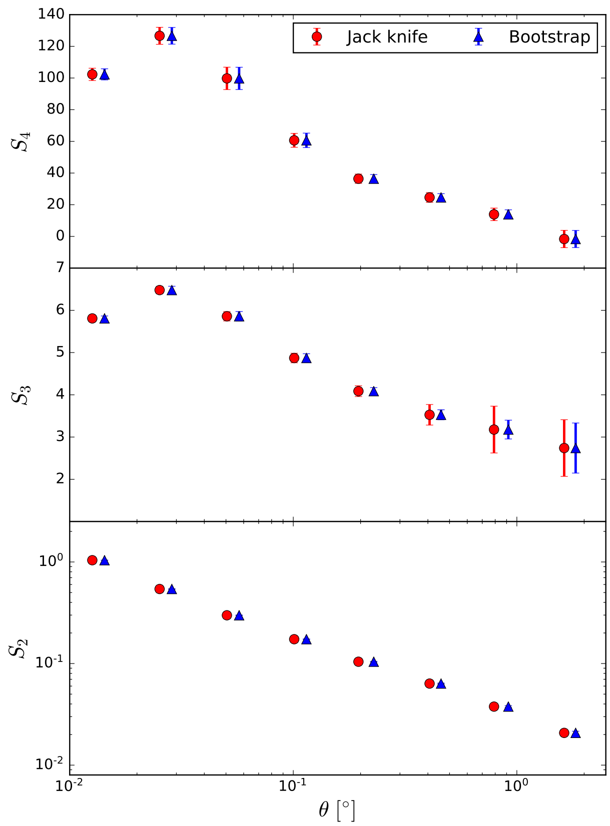

Figure 3. Moments of the density contrast distribution as a function of cell scale in the MICE simulation for the redshift bin $0.2 < z < 0.4$, with jackknife errors (red) and bootstrap errors (blue). The results for a given scale θ have been separated in the figure for visualization purposes, being the blue triangles the ones shown at the nominal measured scale.

cell and thus on the shape that we choose for the pixels. In Gaztañaga (1994), the authors estimate CiC for square cells of side l in a range $l = 0.03° - 20°$ and compare to the average correlation functions $\overline{w}_2(\theta)$. The agreement between the two estimates indicates that square cells give very similar results to circular cells when the sizes of the cells are scaled to $\theta = l/\sqrt{\pi}$. Using data from MICE, we perform several tests to see that the concrete shape of the pixel, when it is close to a regular polygon, does not affect the measured moments despite boundary effects (Appendix B). Furthermore, when working with the acquired observational data, the geometry of the survey becomes complicated. A discussion of how we deal with this is found in Appendix C. The error bars throughout this paper, are estimated using the bootstrap method (Efron 1979; Ivezić et al. 2014). This choice is mainly due to the lack of number of samples for large pixel sizes that might limit the precision of other methods such as jack-knife, given that the latter depends highly on the number of samples as pointed out in (Norberg et al. 2009). Figure 3 shows agreement between the uncertainties computed using the jackknife and bootstrap methods for a randomly chosen redshift bin in the MICE simulation.

3.2 Galaxy bias

One of the most important applications of the CiC observable is the determination of the galaxy bias. We observe the galaxy distribution and use it as a proxy to the underlying matter distribution. Both baryons and dark matter structures grow around primordial overdensities via gravitational interaction, so these distributions should be highly correlated. This relationship is called the *galaxy bias*, which measures how well galaxies trace the dark matter. Galaxy biasing was seen for the first time analyzing the clustering of different populations of galaxies (Davis et al. 1978; Dressler 1980). The theoretical relation between galaxy and mass distributions was suggested by Kaiser (1984) and developed by Bardeen et al. (1986). Since then, many different prescriptions have arisen (Fry & Gaztañaga 1993; Bernardeau 1996; Mo & White 1996; Sheth & Tormen 1999; Manera et al. 2010; Manera & Gaztañaga 2011). However, there is no generally accepted framework for galaxy biasing. While the galaxy and dark matter distribution are related, the exact relation depends on galaxy formation (Press & Schechter 1974), galaxy evolution (Nusser & Davis 1994; Tegmark & Peebles 1998; Blanton et al. 2000), and selection effects. Bias depends strongly on the environment. Using dark matter simulations, the authors in Pujol et al. (2017) show how the halo bias is determined by local density and not by halo mass. Several studies have demonstrated the different behaviors of early-type and late-type galaxies at both small and large scales (Ross et al. 2006; Willmer et al. 1999; Zehavi et al. 2002; Norberg et al. 2002). To have a good estimate of the real matter distribution, it is convenient to use a galaxy sample as homogeneous as possible. With the linear bias $b(z)$ approximation, we can relate the matter fluctuations δ_m with the fluctuations in the galaxy distribution δ_g:

$$\delta_g = b\delta_m \tag{9}$$

In the linear approximation, up to scalings, all statistical properties are preserved by the biasing and the observed galaxy properties reflect the matter distribution on large scales, as long as we consider only two-point statistics. However, in the general case, it is highly unlikely that the relation is both local and linear. Non-local dependencies might come from some properties such as the local velocity field or derivatives of the local gravitational potential (Fry & Gaztañaga 1993; Scherrer & Weinberg 1998). Bias also depends on redshift (Fry 1996; Tegmark & Peebles 1998). When non-Gaussianities are taken into account, linear bias fails to be a good description. If we want to measure higher orders we can assume that the (smoothed) galaxy density can be written as a function of the mass density and expand it as a Taylor series (assuming a local relation) (Frieman & Gaztañaga 1999; Fry & Gaztañaga 1993):

$$\delta_g = f(\delta) = \sum_{k=0}^{\infty} \frac{b_k}{k!} \delta_m^k \tag{10}$$

The linear term $b_1 = b$ is the usual linear bias. Using this expansion we can relate the dark matter and the galaxy density contrast moments using the following relationships (Fry & Gaztañaga 1993):

$$S_2 = b^2 S_{2m} \tag{11}$$

$$S_3 = b^{-1}(S_{3m} + 3c_2) \tag{12}$$

$$S_4 = b^{-2}(S_{4m} + 12c_2S_{3m} + 4c_3 + 12c_2^2) \quad (13)$$

where $c_k = b_k/b$ for $k \geqslant 2$. We will refer to this model as **local**.

The authors in Bel et al. (2015) point out that ignoring the contribution from the non-local bias can affect the linear and non-linear bias results. As a consequence, we analyze the case when the non-local contribution is included. To do so, we substitute c_2 by $c_2' = c_2 - \frac{2}{3}\gamma_2$, where γ_2 is the so-called non-local bias parameter (Bel et al. 2015). We will refer to this model as **non-local**.

Note that we omit the terms higher than 3rd order because, as we will show later, we have very limited sensitivity to b_3, and expect to have no sensitivity to b_4.

3.3 Estimating the projected linear and non-linear bias

The relations in equations (11-13) refer to the three-dimensional case and connect an observed galaxy distribution with its underlying dark matter distribution, both tracing the same redshift range and cosmological parameters. We assume that this bias model is also valid for the projected moments (we will check the validity of this assumption later). Moreover, given the measurements in a dark matter simulation with the same redshift distribution and angular footprint as our galaxy dataset, we estimate the linear and non-linear bias of these galaxies using equations (11-13). Note that these relations apply when we are comparing two datasets with the same value for σ_8 parameter. In the case that $\sigma_8 \neq \sigma_{8,m}$ we will have to correct the resulting bias so,

$$b_{corr} = b_{uncorr}\frac{\sigma_{8,m}}{\sigma_8}. \quad (14)$$

We will use this correction in Section 6.3. We also take advantage of the fact that the skewness and kurtosis depend weakly with the cosmological parameters (Bouchet et al. 1992). In particular, a 5% variation choosing $\Omega_m = 0.25$ translates to a variation of 0.2% in the measured S_{3m}, which is much smaller than the statistical fluctuations that we expect from our samples. In the case of S_{4m} our sensitivity is even lower, making it safe to use a simulation with the same footprint and redshift distribution, as long as the variation in the cosmological parameters is small. However, this is not necessarily true for the case of S_{2m}, where the dependency on the cosmological parameters is higher. We check this using equation (8) to compute the projected S_{2m} for two different sets of cosmological parameters: our fiducial Planck cosmology (Ade et al. 2014) and a model with $\Omega_m = 0.2$. We use a Gaussian selection function $\phi(z)$ with $\sigma_z = 0.05(1+z)$ since this is representative of the datasets that we analyze in this work. After this, we check the ratio:

$$\delta p_{ij}(z,\theta) = \frac{S_{2m,i}(z,\theta)}{S_{2m,j}(z,\theta)}\frac{D^2_{+,j}(\bar{z})}{D^2_{+,i}(\bar{z})} \quad (15)$$

for the different redshift slices considered in our analysis, where the subscripts i and j correspond to two different sets of cosmological parameters and $D_+(\bar{z})$ is the linear growth factor (Peebles 1980; Heath 1977) evaluated at the mean redshift of the considered slice. This gives us an upper limit to the expected variation in S_{2m} to consider in our analysis. In Figure 4 we can see that the variation is within 12% of the linear prediction, thus, we conservatively assign 12%

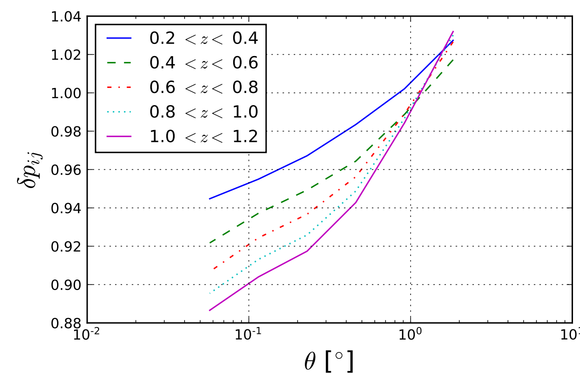

Figure 4. Effect of the variation of Ω_m within Planck priors in S_{2m}. We see that the variation is within 12% of the linear prediction.

systematic error to S_{2m} due to this variation. Under these conditions we perform a simultaneous fit to b, b_2, b_3 and γ_2. In order to do so, we consider the likelihood:

$$\log\mathcal{L} = -\frac{1}{2}\sum_{k=2}^{4}\sum_{i,j}\left[S_{k,g}(\theta_i) - S_{k,mod}(\theta_i)\right] C^{-1}_{k,ij}\left[S_{k,g}(\theta_j) - S_{k,mod}(\theta_j)\right] = -\frac{\chi^2}{2} \quad (16)$$

where $S_{k,g}$ are the measured galaxy moments and $S_{k,mod}$ are the models in equations (11), (12), and (13). We checked that the measured S_k follow a Gaussian distribution. The covariances $C_{k,ij}$ are computed as follows:

$$C_{k,ij} = \frac{N_{u,pix}(\theta_i)}{N_{u,pix}(\theta_j)}2^{2(j-i)}\sigma_k(\theta_i)\sigma_k(\theta_j) \quad (17)$$

with $N_{u,pix}(\theta_i)$ being the number of pixels used in an aperture, θ_i. Note that, since we are using `HEALPix`, and we are not displacing the field, we are re-using the same galaxies for different scales, so the factor $\frac{N_{u,pix}(\theta_i)}{N_{u,pix}(\theta_j)}2^{2(j-i)}$ accounts for the induced correlation due this reuse. We assume that the errors in the dark matter moments and the errors in the galaxy moments are not correlated and add them in quadrature, so:

$$\sigma_k(\theta_i) = \sqrt{\sigma^2_{k,gal}(\theta_i) + \sigma^2_{k,m}(\theta_i)} \quad (18)$$

where $\sigma_{k,gal/m}(\theta_i)$ is the standard deviation of the k-th (galaxy or matter) moment in an aperture θ_i computed using bootstrapping.

We use the following flat priors:

- $0 < b < 10$.
- $-10 < b_2 < 10$.
- $-10 < b_3 < 10$.
- $\gamma_2 = 0$ (or in the case of non-local model $-10 < \gamma_2 < 10$).

These priors have been chosen to prevent unphysical results. We evaluate the likelihood and obtain the best fit values and their uncertainties by performing a MCMC using the software package `emcee` (Foreman-Mackey et al. 2013). Summarizing, the method works as follows:

(i) Measure CiC moments using `HEALPix` pixels in the galaxy sample.
(ii) Measure CiC moments using the same pixels and selection function in a dark matter simulation with comparable cosmological parameters.
(iii) Evaluate statistical and systematic uncertainties in the measured moments.
(iv) Obtain best fit b, b_2, b_3, (and γ_2 in the non-local model) using MCMC with the models from equations (11-13).

In summary, in the local model we fit 3 free parameters, whereas in the non-local model we fit 4.

In Hoffmann et al. (2015), the authors present a prediction for the non-linear bias as a function of the linear bias in the three-dimensional case:

$$b_2 = b^2 - 2.45b + 1.03 \quad (19)$$

$$b_3 = b^3 - 7.32b^2 + 10.79b - 3.90 \quad (20)$$

We will use these predictions to test the compatibility between the 3D and the measured projected values for the non-linear bias.

4 RESULTS IN SIMULATIONS

In order to validate this method, we first compute the CiC moments in the MICE simulation (in both galaxies and DM) using a Gaussian selection function $\phi(z)$ with $\sigma_z = 0.05(1+z)$. This σ_z is similar to the photometric redshifts found in the data using TPZ (Carrasco Kind & Brunner 2013) and BPZ (Benitez 2000). We split our sample into 5 photometric redshift bins: $z \in [0.2, 0.4], [0.4, 0.6], [0.6, 0.8], [0.8, 1.0], [1.0, 1.2]$, mirroring the choice in (Crocce et al. 2016). Then we do the same with the SV data sample presented in Section 2.2 with TPZ photometric redshifts.

4.1 Angular moments for MICE

Figure 5 shows the moments of the density contrast distribution as a function of the cell scale for the different photometric redshift bins. We observe that the moments follow the expected trend, that is, lower redshift bins have higher values for the higher-order moments since non-linear gravitational collapse has a larger effect on these. This is true for all measurements except for the last two redshift bins of the variance, S_2. This can be due to the magnitude cuts, since the galaxy populations are different at different redshifts. We also see that the larger the cell scale, the smaller the variance S_2, since larger cell scales should be more homogeneous. The skewness and the kurtosis in linear scales ($\theta > 0.1°$) are constant and of the same order of magnitude as the expected values ($S_3 \approx 34/7$, $S_4 \approx 60712/1323$) (Bernardeau 1994). The behavior at non-linear scales is due to the non-linearities of the MICE simulation.

4.2 Projected galaxy bias in MICE simulation

We smear the true redshift with the proper selection function in the MICE dark matter field, obtained from a dilution of the dark matter particles (taking 1/700 of the particles). The authors in Chang et al. (2016) demonstrate that the dilution of the dark matter field does not impact their statistics and using the measured moments from the previous section we proceed to perform a simultaneous fit for b, b_2, and b_3 using the local, non-linear bias model from equations (11,12,13). The fit results are summarized in Figure 6. We can see the impact of changing the range of θ considered in the fit. In this case we see that including scales smaller than $0.1°$, where non-linear clustering has a large impact, affects the b_2 results. This, together with the fact that the reduced χ^2 minimum value doubles when including $\theta = 0.05°$ clearly shows that we should not consider scales smaller than $\theta = 0.1°$. We can see as well that b_3 is compatible with zero and that we have a limited sensitivity to it, given the area used. Thus, the choice of ignoring terms of orders higher than b_3 becomes a good approximation. However, for b_2 we are able to measure a significant non-zero contribution. We can also see that the predicted values for the 3D non-linear bias parameter b_2 are not in good agreement at small scales, while there is an indication of better agreement at larger scales. This suggests that the 2D and 3D values for b_2 might be compatible at larger scales, in agreement with Manera & Gaztañaga (2011) who show that the local bias is consistent for scales larger than $R > 30 - 60$ Mpc/h. They also show that the values of b_1

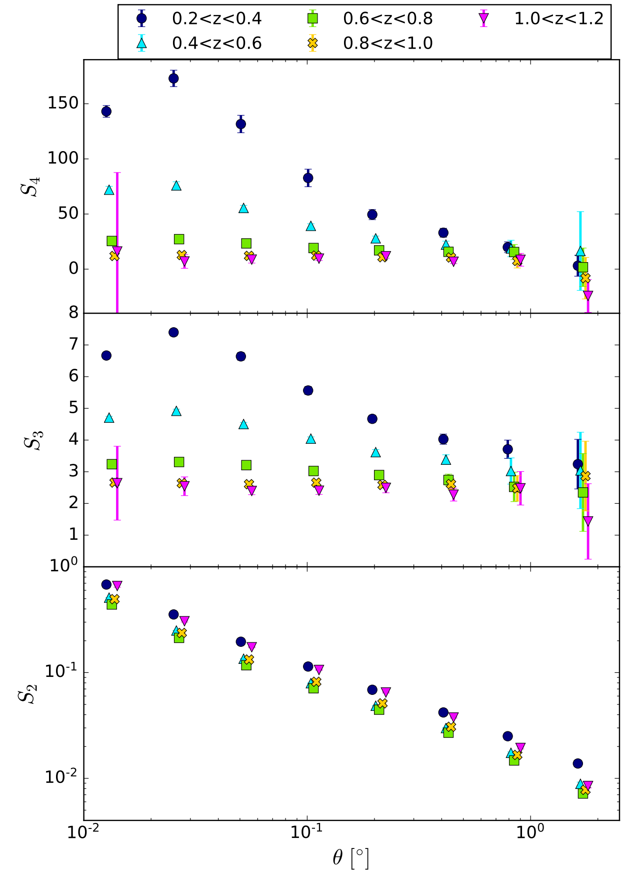

Figure 5. Moments of the density contrast distribution as a function of cell scale in the MICE simulation with Gaussian photometric redshift ($\Delta z = 0.2$ $\sigma_z = 0.05(1+z)$) for different redshift bins. The results for a given scale θ have been separated in the figure for visualization purposes.

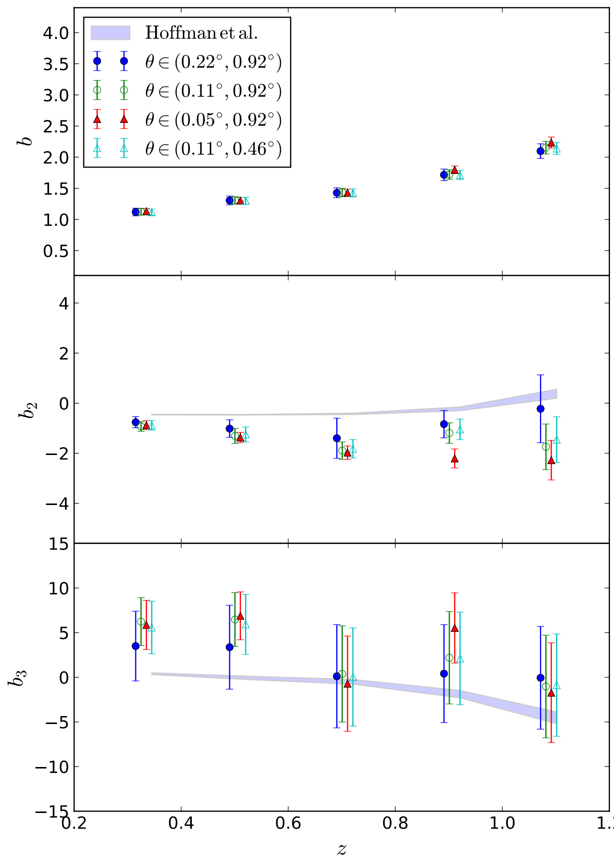

Figure 6. Linear and non-linear bias results as a function of redshift for MICE data with Gaussian photo-z. The different colors represent the best-fit results considering different ranges of the aperture angle θ. In red (solid triangles) we consider the range from 0.05° to 0.92°, green (open circles) is our fiducial case with $0.11° < \theta < 0.92°$, in blue (solid circles) we take out the smallest scale in our fiducial case and in cyan (open triangles) we take out the largest scale. The top panel shows the projected linear bias b as a function of redshift, the middle panel shows the best-fit results for the projected b_2, and b_3 is shown in the lower panel. The shaded region corresponds to the 3D predicted values using equations (20). The results for a given redshift z have been separated in the figure for visualization purposes.

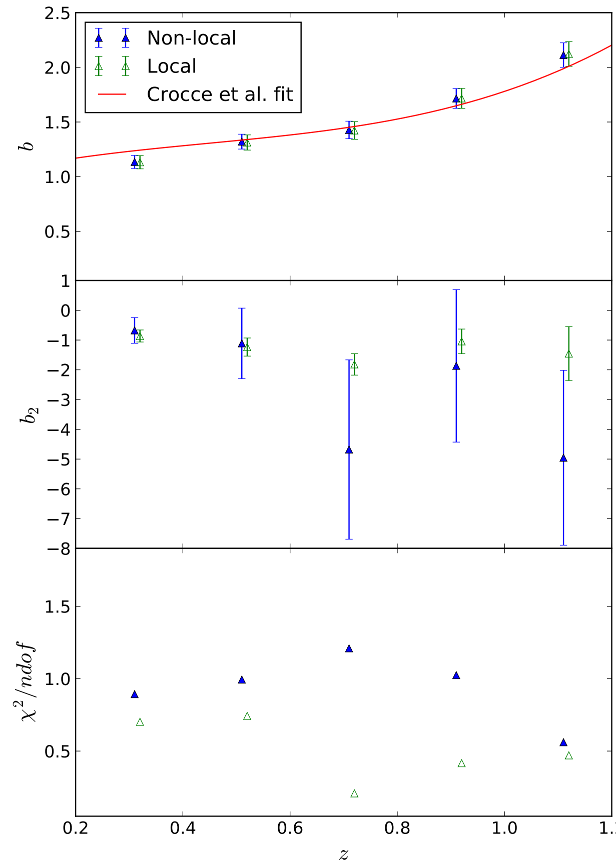

Figure 7. (Top) Comparison between the MICE simulation bias obtained using CiC with different biasing models: non-local (solid triangles), and local (open triangles). We also show the best-fit from Crocce et al. (2016) (Figure 17) as reference. The middle panel shows the equivalent results for b_2. This is done for Gaussian photo-z with $\sigma_z = 0.05(1+z)$. (Bottom) total reduced chi-square for each of the models when fitting the moments to obtain the bias.

and b_2 vary with the scale and converge to a constant value around $R > 30 - 60$ Mpc/h, which means that the values that we measure here have not yet fully converged. The prediction for b_3 seems to be compatible with the estimated values given the size of the error bars. These results show that we should consider b_2 as a first order (small) correction to the linear bias model at these scales for projected (angular) measurements. The individual fits can be seen in Appendix D.

4.3 Verification and biasing model comparison

In order to verify this method and check if the local non-linear model considered induces certain systematic biases on the results, we check that the measured linear bias is compatible with corresponding measurements from the two point correlation function (Figure 7). In particular, we use the best fit parametrization from Crocce et al. (2016):

$$b_{best}(z) = 0.98 + 1.24z - 1.72z^2 + 1.28z^3 \qquad (21)$$

In Figure 7, we can see that the local and non-local bias are in agreement, most likely due to the scale range that we are dealing with and the projection effects due to the size of the redshift slices. We can also see that the simplest model (local) has the lowest reduced chi square.

5 RESULTS IN DES-SV DATA

5.1 Angular moments for DES - SV

Using the same footprint, selection cuts, and redshift bins as in Crocce et al. (2016), we compute the moments of the density contrast distribution for the SV data. These results are depicted in Figure 8 as a function of cell scale for different redshift bins. Here, as in the case of MICE, the variance decreases with the scale. The skewness and the kurtosis are also constant and of the same order of magnitude as the theoretical values within errors. The largest differences when compared with the simulation are in the non-linear regime due

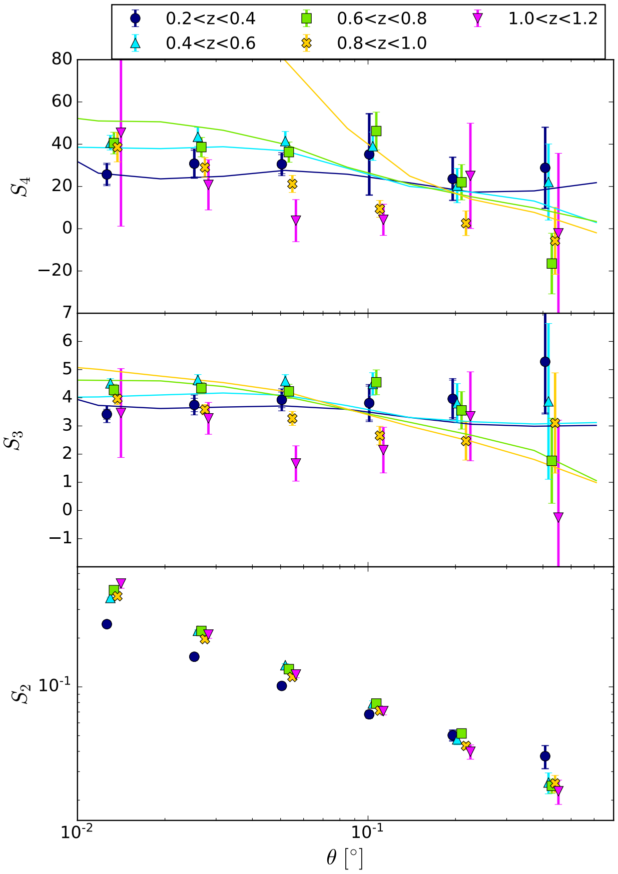

Figure 8. Moments of the density contrast distribution of the DES SV benchmark sample as a function of cell scale, for five different redshift bins and different scales. The results for a given scale θ have been separated in the figure for visualization purposes. We compare with the results from Wolk et al. (2013) for CFHTLS marked with solid lines of different colors for the different redshift bins: navy ($0.2 < z < 0.4$), cyan ($0.4 < z < 0.6$), lime ($0.6 < z < 0.8$), yellow ($0.8 < z < 1.0$).

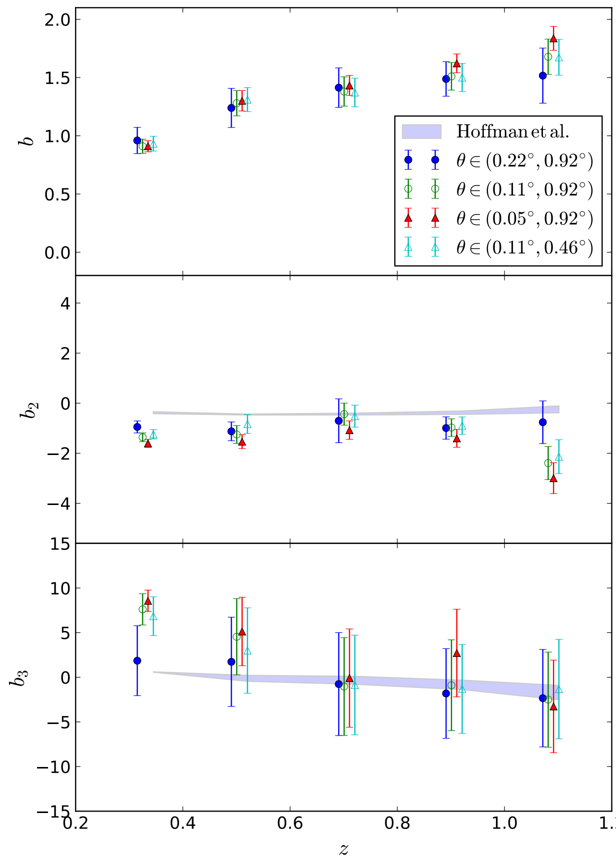

Figure 9. Linear and non-linear bias results as a function of redshift for DES-SV data. Systematic uncertainties from Section 6 are already included in these results, excluding the uncertainties associated to the modeling. The different colors represent the best-fit results considering different ranges of aperture angle θ. In red (solid triangle) we consider the range from 0.05° to 0.92°, green (open circle) is our fiducial case with $0.11° < \theta < 0.92°$, in blue (solid circle) we take out the smallest scale in our fiducial case and in cyan we take out the largest scale (open triangle). The shadowed region corresponds to the 3D predicted values using equations (20). The top panel shows the projected linear bias b as a function of redshift, the middle panel shows the best-fit results for the projected b_2 and b_3 is shown in the lower panel. The results for a given redshift z have been separated in the figure for visualization purposes.

to the different way non-linearities are induced in the simulation and in real data. We also compare to the results from CFHTLS found in Wolk et al. (2013). We find a similar general behavior, as well as the same order of magnitude in the measured S_3 and S_4. However, we do not expect the same exact results since the redshift distributions from CFHTLS do not match exactly the corresponding distributions in the DES-SV data.

5.2 Projected galaxy bias in DES - SV

Repeating the procedure that we used for the MICE galaxy simulation, we analyze the DES - SV data and the MICE dark matter simulation, and compare their moments. In Figure 9 we can see the results of simultaneously fitting for b, b_2 and b_3. The measurements in this figure include the systematic uncertainties are introduced in Section 6. The resulting b is corrected by the ratio of σ_8 between MICE and our adopted fiducial cosmology using equation (14). The fit results can be seen in Figure D2. In this case, we detect a non-zero value for b_2. We check the probability of b_2 being zero by computing:

$$\chi^2_z = \sum_{i,j=1,N_{zbins}} \hat{b}_{2,i} \mathcal{C}^{-1}_{2,ij}(z) \hat{b}_{2,j} \tag{22}$$

The sum runs for all the redshift bins. $\hat{b}_2$ is the weighted average of the fit results with the different fitting ranges and $\mathcal{C}_{2,ij}(z)$ is the covariance matrix for b_2. Taking into account the correlations between different redshift bins:

$$\mathcal{C}_{2,ij}(z) = \frac{N_{ij} N_{ji}}{N_{ii} N_{jj}} \Delta\hat{b}_{2,i} \Delta\hat{b}_{2,j} \tag{23}$$

with N_{ij} is the number of galaxies observed in the photo-z bin i from the true-z bin j and $\Delta\hat{b}_{2,i}$ is the weighted uncertainty in $\hat{b}_{2,i}$ for the photo-z bin i. The value of $\chi^2_z = 64.75$ with 4 degrees of freedom, so the probability is essentially 0, making clear that the overall value of b_2 is non-zero for

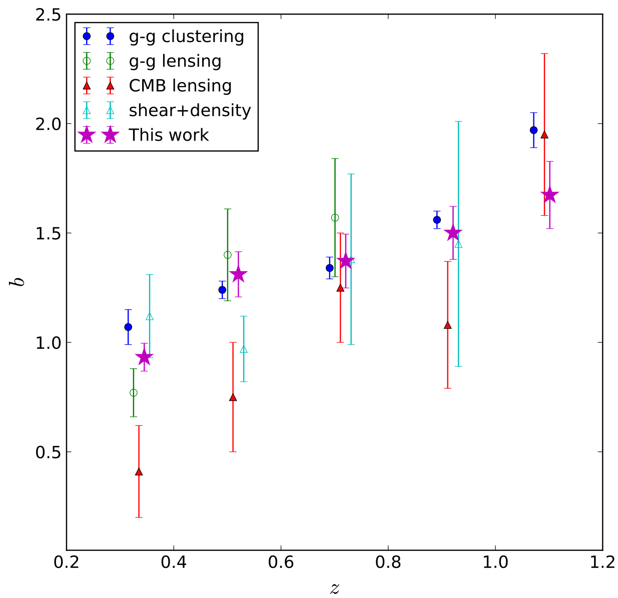

Figure 10. Bias obtained from second order CiC, including systematic uncertainties from Section 6, compared with the 2-point correlation study (Crocce et al. 2016), the CMB-galaxy cross-correlations study (Giannantonio et al. 2016), galaxy-galaxy lensing (Prat et al. 2018), and the shear+density analysis (Chang et al. 2016). The points for the same z have been separated in the horizontal axis for visualization purposes.

the local model. However, we lack the sensitivity necessary to detect a non-zero b_3.

We also check the measurement of linear bias obtained in this work and compare it with previous measurements on the same dataset Figure 10. The measurements are generally in good agreement with each other showing the robustness of the method.

Future DES data will have a considerably larger area and, as previous MICE measurements show, these measurements will improve. Here we also use the skewness and the kurtosis of dark matter from the MICE dark matter simulation, as those quantities hardly depend on the cosmology (Bouchet et al. 1992). We also find that our results are similar to those in Ross et al. (2006). We do not expect them to be equal as the samples are different and the bias depends strongly on the population sample.

6 SYSTEMATIC ERRORS

In this section, we explore the effects that several potential sources of systematic uncertainty have on our moment measurements. Since our main observable is related to the number of galaxy-counts in a given redshift interval, we are interested in observational effects that can affect this number. The main potential sources of systematic uncertainties are changes in airmass, seeing, sky brightness, star-galaxy separation, galactic extinction, and the possible errors in the determination of the photometric redshift. In order to evaluate their effects, we use the maps introduced in Leistedt et al. (2016). To account for the stellar abundance in our field we proceed as in Crocce et al. (2016) and use the USNO-B1 catalog (Monet et al. 2003). We also use the SFD dust maps (Schlegel et al. 1998). What follows is a detailed step-by-step guide to our systematic analysis: we select one of the aforementioned maps and locate the pixels where the value of the systematic is below the percentile level t. We compute the moments of the density contrast distribution in these pixels and their respective errors using bootstrap. We change the threshold to $t+5$, repeat the process, and evaluate the difference between the moments calculated using this threshold divided by the moments in the original footprint $\Delta S_i(t)/\langle S_i \rangle$. An example of the results of this procedure can be found in Figure 11.

We consider that a systematic effect is present if the average of $\Delta S_i(t)/\langle S_i \rangle$ is different from zero at a 2σ confidence level or above for the different values of t from the 50th tile to the 100th tile. Then, we assign a systematic uncertainty equal to the value of this average. To be conservative, we consider these effects as independent, so we add them in quadrature. We summarize the main systematic effects observed in each redshift bin of our sample:

- Bin $0.2 < z < 0.4$:

  – Seeing in i-band: we assign a 3% systematic uncertainty in S_4.
  – Seeing in z-band: we assign a 2.5% systematic uncertainty in S_4.
  – Sky-brightness r-band: we assign a 1% systematic uncertainty in S_4.
  – Sky-brightness i-band: we assign a 1% systematic uncertainty in S_4.
  – Airmass in g-band: we assign a 1% uncertainty in S_4.
  – Airmass in r-band: we assign a 1% uncertainty in S_4.
  – Airmass in i-band: we assign a 1% uncertainty in S_4.
  – USNO-B stars: We assign a 4% uncertainty to S_2, 7% uncertainty to S_3, and 9% to S_4.

- Bin $0.4 < z < 0.6$:

  – Seeing in z-band: We assign a 1.5% uncertainty to S_4.
  – USNO-B stars: We assign a 4% uncertainty to S_2, 3% uncertainty to S_3, and 4% to S_4.

- Bin $0.6 < z < 0.8$:

  – Seeing in g-band: We assign a 2% to S_4.
  – Seeing in r-band: We assign a 2% to S_4.
  – Sky-brightness i-band: We assign a 1.5% uncertainty to S_3, and 3% systematic uncertainty to S_4.
  – Airmass in g-band: We assign a 2.5% uncertainty to S_4.
  – Airmass in r-band: We assign a 2% uncertainty to S_4.
  – Airmass in z-band: We assign a 1.5% uncertainty to S_3, and 3% uncertainty to S_4.
  – USNO-B stars: We assign a 3% uncertainty to S_3, and 5% uncertainty to S_4.

- Bin $0.8 < z < 1.0$:

  – Seeing in g-band: We assign a 2% uncertainty to S_4.
  – Sky-brightness in i-band: We assign a 2% uncertainty to S_3, and a 3.5% uncertainty to S_4.
  – Airmass in g-band: We assign a 2% uncertainty to S_4.
  – Airmass in r-band: We assign a 3% uncertainty to S_4.
  – USNO-B stars: We assign a 3% uncertainty to S_4.

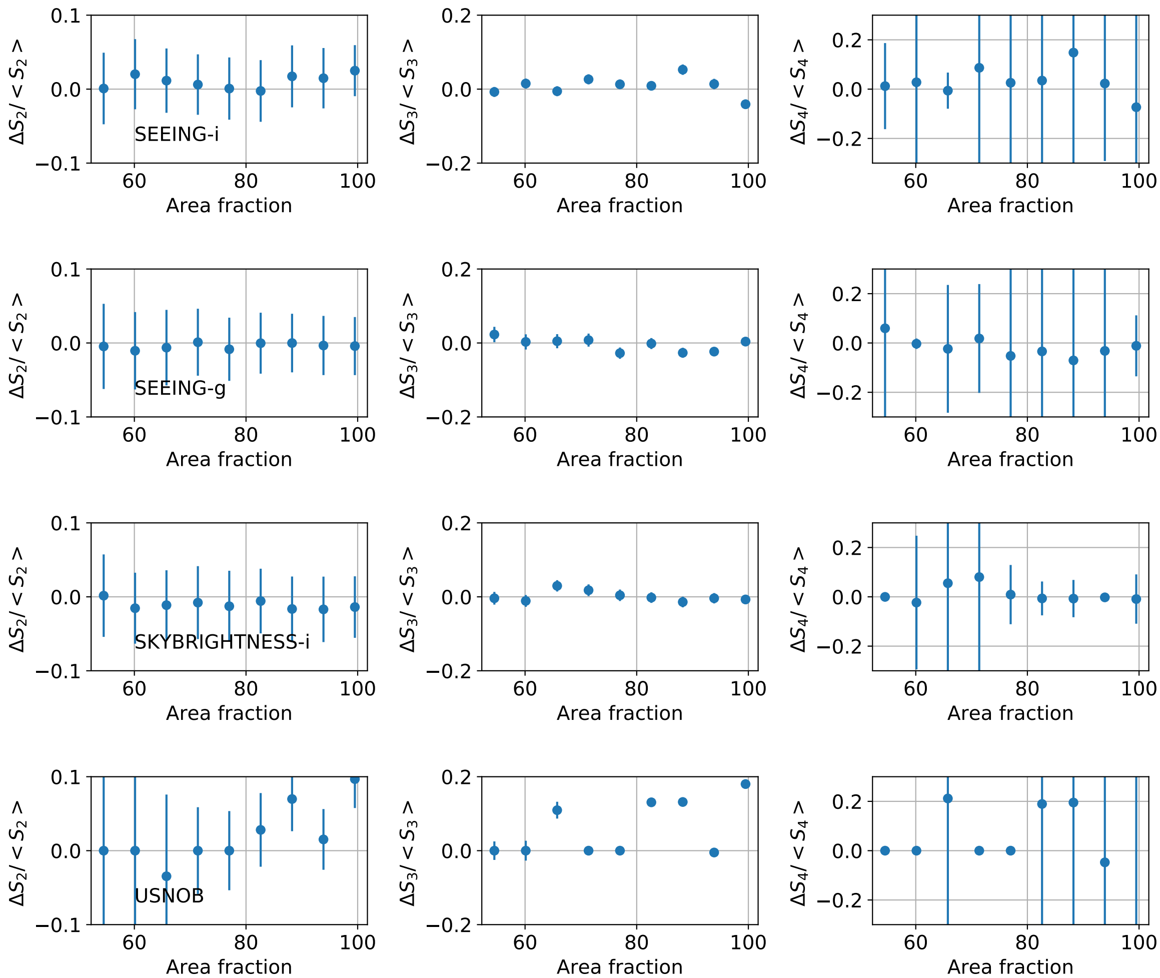

Figure 11. Dependence of the moments S_i with the variation in the value of potential systematic effects. We show an example for $N_{side} = 2048$ in the redshift bin $0.2 < z < 0.4$ using TPZ. The left column shows the behavior for S_2, the middle column shows S_3, and the last column shows the results for S_4. The first row corresponds to the results for the seeing in i-band, the second row shows the results for seeing in g-band, the third shows the sky-brightness in i-band. Finally the last row shows the evolution of the moments with the variation in the number of stars per pixel.

- Bin $1.0 < z < 1.2$:

  – The measurement of S_4 in this bin is dominated by systematics.
  – Sky-brightness i-band: We assign 2% to S_3.
  – Sky-brightness z-band: We assign 3% to S_3.
  – USNO-B stars: We assign a 4.5% uncertainty to S_3.

The estimated systematic errors for the bias are propagated from the estimation of the systematics in S_2, S_3, and S_4. Their behavior is compatible with the systematics found in Crocce et al. (2016). We use the same data masking, excluding regions with large systematic values to recover $w(\theta)$. The linear bias is more robust using CiC since the variance, S_2, is less affected by the small scale power induced by the systematics given that these scales are smoothed out. On the other hand, the non-linear bias is more sensitive to the presence of systematics because they can induce asymmetries in the density contrast distribution.

6.1 Photometric redshift

Photometric redshift is one of the main potential sources for systematic effects in photometric surveys like DES. We have repeated the analysis in DES-SV data for a second estimate of the photometric redshift using BPZ (Benitez 2000). In Figure 12 we compare the results for the two photometric redshift codes and we see that they are in good agreement. The linear bias seems to be the most affected by the choice of a photometric redshift estimator but the results do not show any potential systematic biases. For the non-linear bias we get remarkably consistent results, showing the robustness of this method.

6.2 Biasing models

Apart from the terms that we considered in our model, the authors in Bel et al. (2015) found that non-local bias terms are responsible for the overestimation of the linear bias from the three-point correlation in Pollack et al. (2014); Hoff-

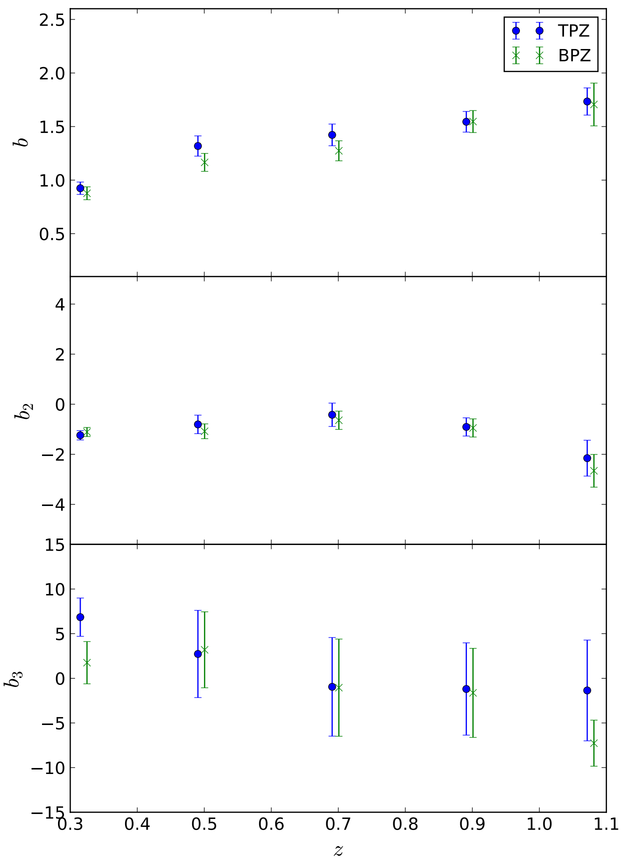

Figure 12. Bias obtained in the SV data from second order CiC for TPZ (solid blue circles) and BPZ (green crosses). The results for a given redshift z have been separated in the figure for visualization purposes.

Bias model	χ^2	p-value	ndof
Local	64.75	3×10^{-13}	4
Non-local	12.63	0.013	4

Table 1. Comparison on the null hypothesis for b_2 in DES-SV data for the different bias models considered in this work.

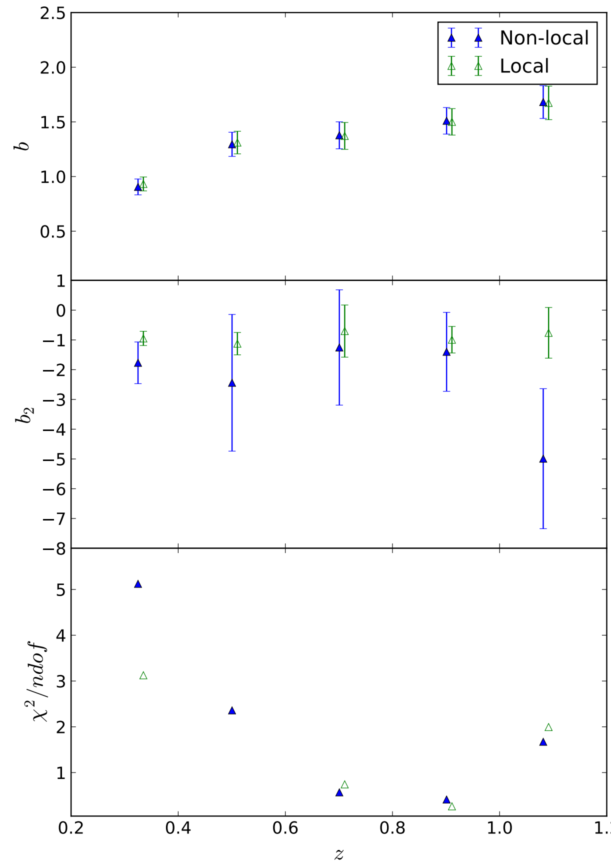

Figure 13. (Top) Comparison between the linear bias results obtained with CiC for SV using different biasing models: non-local (solid triangles), and local (open triangles) using the TPZ sample. (Middle) Comparison between b_2 results for the same models as above. (Bottom) total reduced chi square for each of the models.

mann et al. (2015); Manera & Gaztañaga (2011) but that they should not significantly affect second-order statistics. As we mentioned previously in Section 5, we do not expect these terms to have a significant impact on our estimations because we analyze projected quantities over considerable volumes (note that we integrate in the cell and in the redshift slice). Having said that, we test the local and non-local models and find the results depicted in Figure 13. We can see, as in the case of the simulation, that both models are consistent within errors. This means that choosing the local model does not introduce any systematic uncertainties in our linear bias measurements. However, it affects the b_2 measurements and their uncertainty since the new parameters introduced with these more complicated models are correlated with them. We check the probability of b_2 being zero for the different models and obtain the results in table 1. We find b_2 to be different from zero at a 3-σ level in the worst case (non-local). We also can see that in the first bin, none of the models fit the data well, which is not surprising, given that the range of (comoving) scales is very small ($\sim 1 - 20$ Mpc h^{-1}) and non-linear clustering dominates.

Finally, we are not considering stochastic models and we are assuming a Poisson shot-noise (see appendix A). This means that our measured b_2 could be entangled with stochasticity (Pen 1998; Sato & Matsubara 2013). We leave the study of stochasticity to future works.

6.3 Value of σ_8

As mentioned in previous sections, our bias estimation depends linearly on the value of σ_8. Thus, if the actual value of σ_8 is different from our assumed fiducial value, our results will be biased, and we have to correct for the difference using equation 14. This is why, we introduce a systematic uncertainty of 1.4% (the uncertainty level in σ_8 from Ade et al. (2014)) that we add in quadrature to the statistical errors in the final estimation of the bias.

7 CONCLUSIONS

CiC is a simple but effective method to obtain the linear and non-linear bias. A good measurement of the galaxy bias is essential to maximize the performance of photometric redshift surveys because it can introduce a systematic effect on the determination of cosmological parameters. The galaxy bias is highly degenerate with other cosmological parameters and an independent method to determine it can break these degeneracies and improve the overall sensitivity to the underlying cosmology. In this paper we have developed a method to extract the bias from CiC. We use the MICE simulation to test our method and then perform measurements on the public Science Verification data from the Dark Energy Survey. The strength of this method is that it is based on a simple observable, the galaxy number counts, and is not demanding computationally.

We check that our linear bias measurement from CiC agrees with the real bias in the MICE simulation. Figure 7 shows an agreement between our measurement and the one obtained using the angular two-point correlation function. We then obtain the linear bias in the SV data and find that it is in agreement with previous bias measurements from other DES analyses. In Figure 10, we see that the CiC values are compatible with the two-point correlation study (Crocce et al. 2016), the CMB-galaxy cross-correlations study (Giannantonio et al. 2016), and the galaxy-galaxy lensing (Prat et al. 2018), and we demonstrate that these results are robust to the addition of new parameters in the biasing model, such as the non-local bias. Finally, we compute the non-linear bias parameters up to third order. We detect a significant non-zero b_2 component. It appears that the 2D and 3D predictions of the non-linear bias are in better agreement at larger scales, as expected. However, given the uncertainties associated with these quantities, it is difficult to draw any conclusions from b_3 despite its compatibility with the expected 3D prediction. When more data is available, we plan to check if we can improve our constraints on b_3 and whether the agreement with the 3D prediction improves as well. The systematic errors are in general lower than the statistical errors, in agreement with the systematic study done by (Crocce et al. 2016).

APPENDIX A: SHOT NOISE CORRECTION

Usually, in the analysis what we estimate are the central moments of the angular counts:

$$m_J(\theta) \equiv \sum_{i=0}^{\infty} (i - \overline{N})^J P_i(\theta) \tag{A1}$$

where $P_i(\theta)$ is the probability of finding i galaxies in a randomly selected cell of solid angle A and $\overline{N} \equiv \sum_i iP_i$ is the average number of galaxies per cell. The galaxy density fluctuation in the cell is:

$$\delta_g = \frac{(i - \overline{N})}{\overline{N}} \tag{A2}$$

and therefore:

$$m_J = \overline{N}^J \langle \delta_g^J \rangle \tag{A3}$$

Ultimately, we want to obtain to estimate the averaged correlation functions $\overline{w}_J(\theta)$ are the connected moments:

$$\mu_J \equiv \overline{N}^J \langle \delta_g^J \rangle_c \tag{A4}$$

We have to correct what we measure, which is $\langle \delta_g^J \rangle$, subtracting the lower order contributions. Up to third order we do not have any contributions but at $J = 4$ we do. The connected part is the contribution to $\langle \delta_1, ..., \delta_j \rangle$ which does not include any conditional probability of lower order. To estimate the connected graphs we introduce a moment-generating function:

$$M(t) = \sum_{j=0}^{\infty} \frac{m_j}{j!} = \langle e^{i\delta} \rangle \tag{A5}$$

where $m_j = \left[\frac{d^j}{dt^j} M(t)\right]_{t=0}$ and the connected moments are:

$$\mu_j = \left[\frac{d^j}{dt^j} \log M(t)\right]_{t=0} \tag{A6}$$

Up to $J = 4$ (Gaztañaga 1994):

$$\begin{aligned} \mu_2 &= m_2 \\ \mu_3 &= m_3 \\ \mu_4 &= m_4 - 3m_2^2 \end{aligned} \tag{A7}$$

Also due to discreteness, $\langle \delta_g^J \rangle_c$ is not a good estimator unless $\overline{N} \gg 1$. We have to subtract the shot noise which affects measurements from $J = 2$ on. We use a Poisson model with generating function $M_{Poisson}(t) = M(e^t - 1)$ to obtain better estimators (Gaztañaga 1994):

$$\begin{aligned} k_2 &= \mu_2 - \overline{N} \\ k_3 &= \mu_3 - 3k_2 - \overline{N} \\ k_4 &= \mu_4 - 7k_2 - \overline{N} \end{aligned} \tag{A8}$$

where terms to the right of μ_J are the shot-noise correction. Then in our case, we subtract the shot noise from what we measure $\langle \delta_g^J \rangle = \frac{m_J}{\overline{N}^J}$:

$$\begin{aligned} \langle \delta^2 \rangle_c &= \frac{k_2}{\overline{N}^2} = \langle \delta_g^2 \rangle - \frac{1}{\overline{N}} \\ \langle \delta^3 \rangle_c &= \frac{k_3}{\overline{N}^3} = \langle \delta_g^3 \rangle - \frac{3}{\overline{N}} \langle \delta^2 \rangle_c - \frac{1}{\overline{N}^2} \\ \langle \delta^4 \rangle_c &= \langle \delta_g^4 \rangle - 3\langle \delta_g^2 \rangle^2 - \frac{7}{\overline{N}^2} \langle \delta^2 \rangle_c - \frac{6}{\overline{N}} \langle \delta^3 \rangle_c - \frac{1}{\overline{N}^3} \end{aligned} \tag{A9}$$

where $\overline{N}$ is $\overline{N} = \frac{N_{\rm gal}^{tot} * A_{\rm pix}}{A_{\rm tot}}$, being $N_{\rm gal}^{tot}$ the total number of galaxies, $A_{\rm tot}$ the total area, and $A_{\rm pix}$ the area of the pixel.

Then the final moments would be:

$$\begin{aligned} S_2 &= \langle\delta^2\rangle_c \\ S_3 &= \frac{\langle\delta^3\rangle_c}{\langle\delta^2\rangle_c^2} \\ S_4 &= \frac{\langle\delta^4\rangle_c}{\langle\delta^2\rangle_c^3} \end{aligned} \tag{A10}$$

APPENDIX B: DIFFERENT PIXEL SHAPES

We check with the MICE simulation in a thin redshift bin ($0.95 < z < 1.05$) that as long as we have regular polygon pixels the difference in the moments of the density contrast is negligible. In Figure B1 we see that the difference is negligible for the more symmetrical pixels and higher for less symmetrical ones. The angular aperture, θ, is estimated as the square root of the pixel area. We compare rectangular pixels with `HEALpix` pixels. We divide the sphere into rectangular pixels taking n_{ra} parts in right ascension, and n_{ct} parts in $\sin\mathrm{dec}$ where the number of pixels is npix=$n_{ra} \cdot n_{ct} = 12 \cdot N_{side} \cdot N_{side}$. We have taken six different pixel shapes numbered from 1 to 6. Pixels number 3 ($n_{ra} = 3N_{side},\ n_{ct} = 4N_{side}$), 4 ($n_{ra} = 4N_{side},\ n_{ct} = 3N_{side}$) and 6 ($n_{ra} = 6N_{side},\ n_{ct} = 2N_{side}$) are close to being squares, but pixels number 1 ($n_{ra} = 12N_{side},\ n_{ct} = 1N_{side}$), 2 ($n_{ra} = 1N_{side},\ n_{ct} = 12N_{side}$) and 5 ($n_{ra} = 2N_{side},\ n_{ct} = 6N_{side}$) are far from being regular polygons. When we compare square and `HEALpix` pixels we see that the measured moments are in perfect agreement.

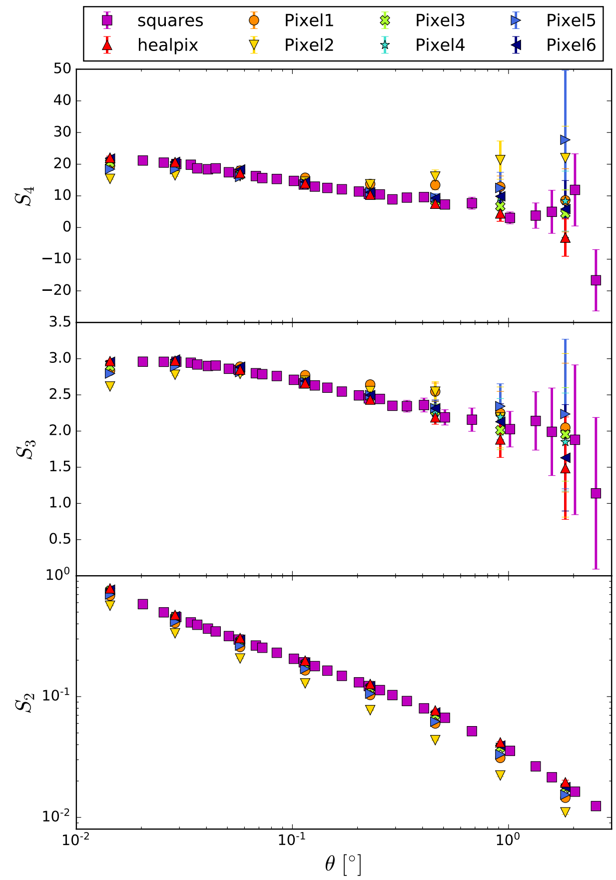

Figure B1. Moments of the density contrast distribution as a function of the cell scale using data from MICE in the redshift slice $0.95 < z < 1.05$ for different pixel shapes. Pixels number 3 ($n_{ra} = 3N_{side},\ n_{ct} = 4N_{side}$), 4 ($n_{ra} = 4N_{side},\ n_{ct} = 3N_{side}$) and 6 ($n_{ra} = 6N_{side},\ n_{ct} = 2N_{side}$) are close to being squares, but pixels number 1 ($n_{ra} = 12N_{side},\ n_{ct} = 1N_{side}$), 2 ($n_{ra} = 1N_{side},\ n_{ct} = 12N_{side}$) and 5 ($n_{ra} = 2N_{side},\ n_{ct} = 6N_{side}$) are far from being regular polygons.

APPENDIX C: BOUNDARY EFFECTS

To deal with the boundary effects of an irregularly shaped area, we use the mask and degrade its resolution to match each of the pixel scales being used. However, degrading the mask (or increasing the scale) results in an increasing number of partially filled pixels. Only a fraction $r_A = A_{\rm filled}/A_{\rm pixel}$ remain completely inside the footprint. This means that, if we assign the same scale to all the pixels of a given N_{side} value, some pixels will be effectively mapping a different scale. To solve this problem we can either require a minimum fraction of the pixel to be full, $r_A \geqslant X$, or we can compute the fraction of full pixels and perform CiC for that scale. We prefer to use the former because we consider that the scales where we perform the study appropriately map the variations of the density field in which we are interested. This approach also helps to avoid certain boundary effects. For small pixel sizes (similar to the size in the mask), given the large number of pixels, we can safely choose $r_A = 1$. For bigger pixels we try to find a compromise between the amount of area that we lose and the boundary effects. In Figures C1 and C2 we show the area loss using data from MICE in the redshift bin $0.95 < z < 1.05$ with the SV mask for different thresholds in r_A and in Figure C3 the change in the moments for these different area cuts. We see that if we choose pixels that are completely contained inside the mask ($r_A = 1.0$), we lose a lot of area for smaller values of N_{side}, however, very little area is lost for large values of N_{side}. It can be seen that results are consistent for the different threshold values for r_A. We also see that if we take all the pixels ($r_A \geqslant 0$), the difference in the moments is considerable in some cases, and we cannot take just all the pixels inside the mask ($r_A = 1$) because we run out of them for large scales. We set a threshold $r_A \geqslant 0.9$ to ensure that the pixels are almost completely embedded in the footprint. This prevents us from mixing scales even for the largest pixel sizes. This can be noted in Figure C1 where a large drop in area occurs between $r_A = 0.8$ and $r_A = 0.9$ for $N_{side} \leqslant 1024$, setting this threshold naturally. For most scales this threshold does not change the errors. By choosing $r_A \geqslant 0.9$ the effective cell sizes are well determined and the errors are reasonably small.

APPENDIX D: SIMULTANEOUS FITS RESULTS

In this section we show the fitting results for the simultaneous fits in MICE. In Figures D1 and D2, the red line corresponds to the mean value of the samples and the grey lines are the different models evaluated by the MCMC.

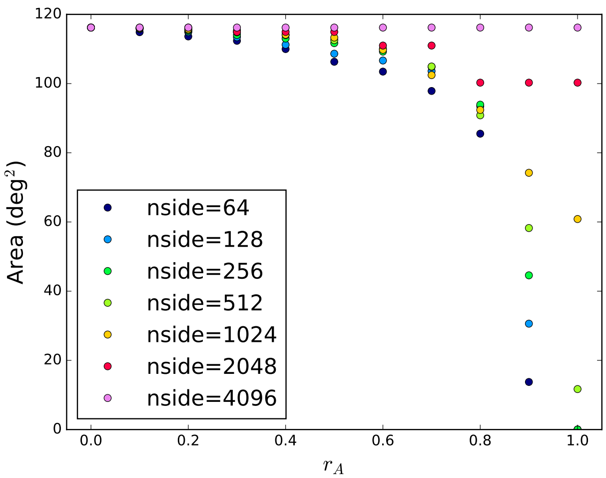

Figure C1. Area covered by different **HEALpix** pixelation resolutions as a function of the minimum fraction of pixel coverage of said resolution with respect to the $N_{side} = 4096$ footprint (larger pixels from lower N_{side} will be partially filled at times). This test is done using the MICE simulation considering the same footprint as the SV dataset.

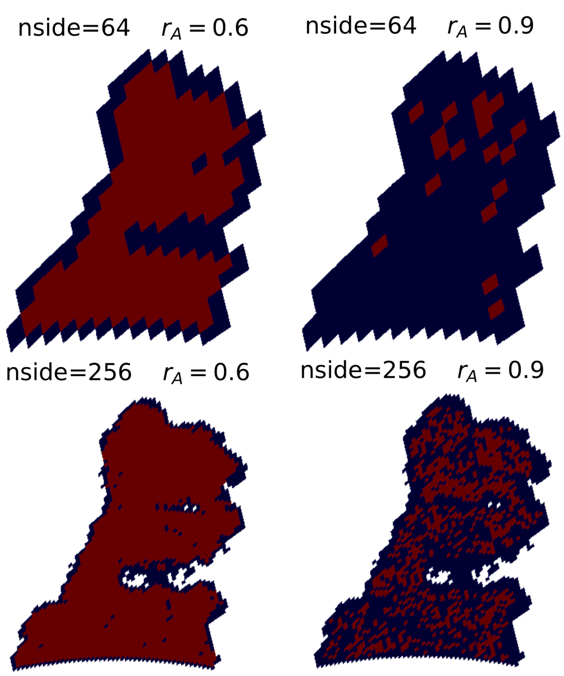

Figure C2. DES SV mask for different N_{side} (64, 256) and different area cuts $r_A = 0.6,\ 0.9$. The pixels that we discard are blue and the ones that we keep are red. The bigger the pixel, the larger the amount of data we lose.

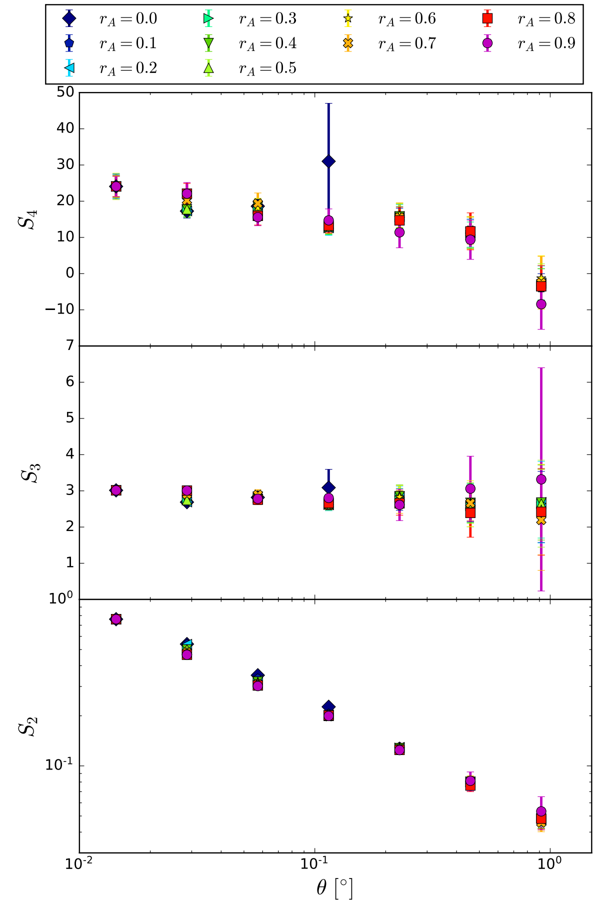

Figure C3. Moments of the density contrast distribution obtained from MICE ($0.95 < z < 1.05$) considering the same footprint as the SV data for different values of the fraction of the pixel inside the mask, r_A. The results for a given scale θ have been separated in the figure for visualization purposes.

AFFILIATIONS

[1] Instituto de Fisica Teorica UAM/CSIC, Universidad Autonoma de Madrid, 28049 Madrid, Spain
[2] Department of Physics and Astronomy, University of California, Irvine, 92602, USA
[3] Centro de Investigaciones Energéticas, Medioambientales y Tecnológicas (CIEMAT), Madrid, Spain
[4] Department of Physics and Astronomy, University of California, Riverside, 92521, USA
[5] Kavli Institute for Cosmological Physics, University of Chicago, Chicago, IL 60637, USA
[6] DEDIP/DAP, IRFU, CEA, Université Paris-Saclay, F-91191 Gif-sur- Yvette, France
[7] Université Paris Diderot, AIM, Sorbonne Paris Cité, CEA, CNRS, F-91191 Gif-sur-Yvette, France
[8] Fermi National Accelerator Laboratory, P. O. Box 500, Batavia, IL 60510, USA
[9] Institut d'Estudis Espacials de Catalunya (IEEC), 08193 Barcelona, Spain
[10] Institute of Space Sciences (ICE, CSIC), Campus UAB, Carrer de Can Magrans, s/n, 08193 Barcelona, Spain
[11] Center for Cosmology and AstroParticle Physics, Department of Physics, The Ohio State University, 191 W Woodruff Ave,Columbus OH 43210, U.S.A.
[12] Cerro Tololo Inter-American Observatory, National Optical Astronomy Observatory, Casilla 603, La Serena, Chile
[13] Institute of Cosmology & Gravitation, University of Portsmouth, Portsmouth, PO1 3FX, UK
[14] CNRS, UMR 7095, Institut d'Astrophysique de Paris, F-75014, Paris, France

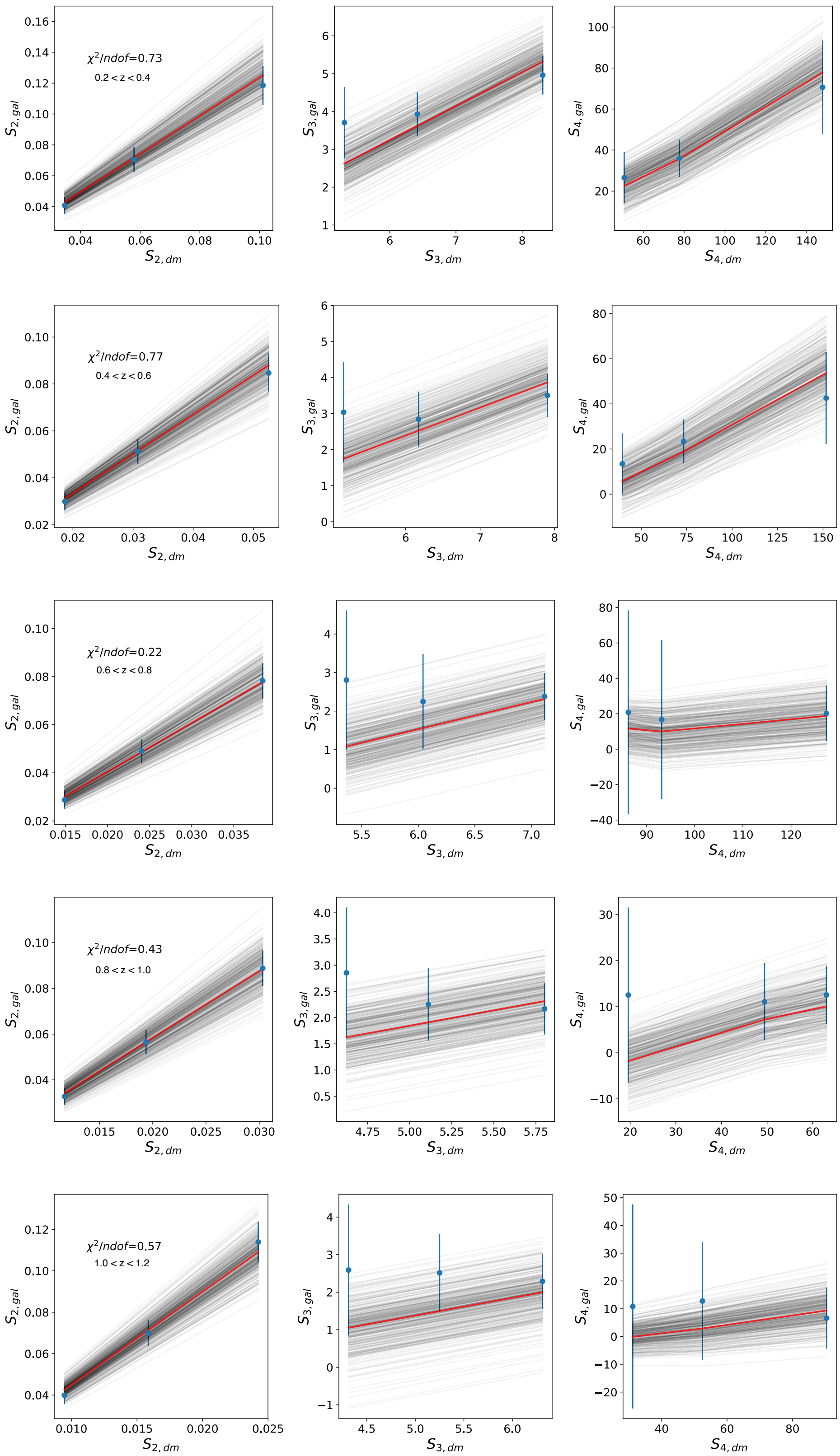

Figure D1. Fit results for the non-linear bias simultaneous fits method using MICE with Gaussian photo-z. The points are the measured moments and the error bars are calculated by adding in quadrature the uncertainties from the moments in the dark matter and the galaxies. The red line is the best-fit curve corresponding to the mean of the posterior distribution. The gray lines are the different models evaluated by the MCMC. The top row corresponds to the first redshift bin ($0.2 < z < 0.4$), the second row corresponds to the second redshift bin, and so on.

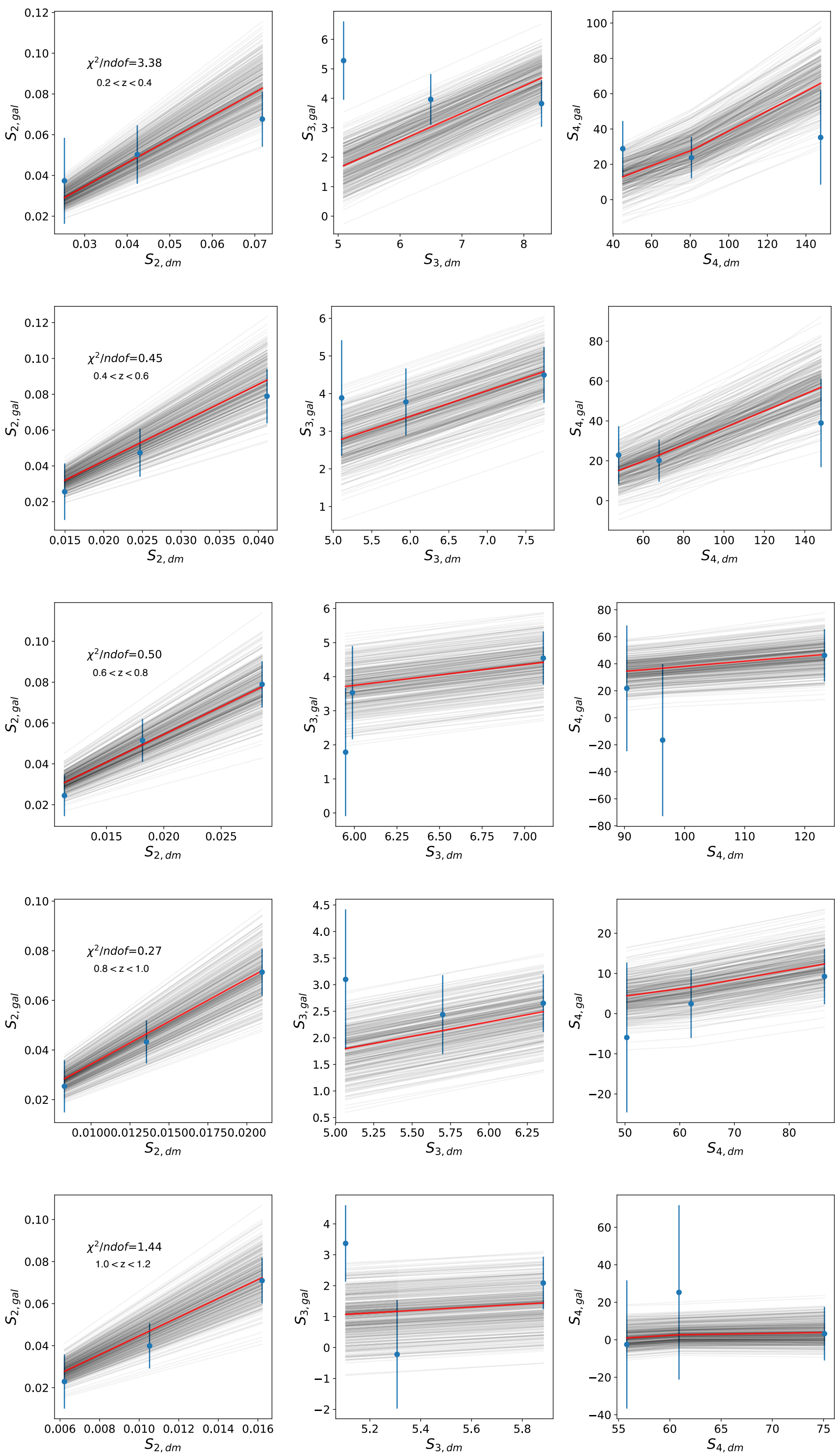

Figure D2. Non-linear bias fits for DES-SV data. See caption in Figure D1 for more details.

[15] Sorbonne Universités, UPMC Univ Paris 06, UMR 7095, Institut d'Astrophysique de Paris, F-75014, Paris, France
[16] Department of Physics & Astronomy, University College London, Gower Street, London, WC1E 6BT, UK
[17] Kavli Institute for Particle Astrophysics & Cosmology, P. O. Box 2450, Stanford University, Stanford, CA 94305, USA
[18] SLAC National Accelerator Laboratory, Menlo Park, CA 94025, USA
[19] Laboratório Interinstitucional de e-Astronomia - LIneA, Rua Gal. José Cristino 77, Rio de Janeiro, RJ - 20921-400, Brazil
[20] Observatório Nacional, Rua Gal. José Cristino 77, Rio de Janeiro, RJ - 20921-400, Brazil
[21] Department of Astronomy, University of Illinois at Urbana-Champaign, 1002 W. Green Street, Urbana, IL 61801, USA
[22] National Center for Supercomputing Applications, 1205 West Clark St., Urbana, IL 61801, USA
[23] Institut de Física d'Altes Energies (IFAE), The Barcelona Institute of Science and Technology, Campus UAB, 08193 Bellaterra (Barcelona) Spain
[24] Department of Astronomy, University of Michigan, Ann Arbor, MI 48109, USA
[25] Department of Physics, University of Michigan, Ann Arbor, MI 48109, USA
[26] Department of Physics, ETH Zurich, Wolfgang-Pauli-Strasse 16, CH-8093 Zurich, Switzerland
[27] Santa Cruz Institute for Particle Physics, Santa Cruz, CA 95064, USA
[28] Harvard-Smithsonian Center for Astrophysics, Cambridge, MA 02138, USA
[29] Australian Astronomical Observatory, North Ryde, NSW 2113, Australia
[30] Departamento de Física Matemática, Instituto de Física, Universidade de São Paulo, CP 66318, São Paulo, SP, 05314-970, Brazil
[31] Department of Physics and Astronomy, University of Pennsylvania, Philadelphia, PA 19104, USA
[32] George P. and Cynthia Woods Mitchell Institute for Fundamental Physics and Astronomy, and Department of Physics and Astronomy, Texas A&M University, College Station, TX 77843, USA
[33] Institució Catalana de Recerca i Estudis Avançats, E-08010 Barcelona, Spain
[34] Department of Physics and Astronomy, Pevensey Building, University of Sussex, Brighton, BN1 9QH, UK
[35] School of Physics and Astronomy, University of Southampton, Southampton, SO17 1BJ, UK
[36] Brandeis University, Physics Department, 415 South Street, Waltham MA 02453
[37] Instituto de Física Gleb Wataghin, Universidade Estadual de Campinas, 13083-859, Campinas, SP, Brazil
[38] Computer Science and Mathematics Division, Oak Ridge National Laboratory, Oak Ridge, TN 37831
[39] Argonne National Laboratory, 9700 South Cass Avenue, Lemont, IL 60439, USA

ACKNOWLEDGEMENTS

We are very grateful to our DES internal reviewers E. Gaztañaga, I. Sevilla, and A. J. Ross for their valuable comments that greatly improved the quality of this work. We thank Santiago Ávila for useful discussions and providing catalogs for preliminary tests. We thank Anna M. Porredon for providing theoretical correlation functions for checking purposes. We also thank T. H. Diehl, D. Gruen, and D. Burke for their useful comments.

We acknowledge the use of data from the MICE simulations, publicly available at `http://www.ice.cat/mice`. We also acknowledge the use of Scipy, Numpy, Astropy, Healpy, emcee and iPython for this work. FJS acknowledges support from the U.S. Department of Energy. Funding for the DES Projects has been provided by the U.S. Department of Energy, the U.S. National Science Foundation, the Ministry of Science and Education of Spain, the Science and Technology Facilities Council of the United Kingdom, the Higher Education Funding Council for England, the National Center for Supercomputing Applications at the University of Illinois at Urbana-Champaign, the Kavli Institute of Cosmological Physics at the University of Chicago, the Center for Cosmology and Astro-Particle Physics at the Ohio State University, the Mitchell Institute for Fundamental Physics and Astronomy at Texas A&M University, Financiadora de Estudos e Projetos, Fundação Carlos Chagas Filho de Amparo à Pesquisa do Estado do Rio de Janeiro, Conselho Nacional de Desenvolvimento Científico e Tecnológico and the Ministério da Ciência, Tecnologia e Inovação, the Deutsche Forschungsgemeinschaft and the Collaborating Institutions in the Dark Energy Survey.

The Collaborating Institutions are Argonne National Laboratory, the University of California at Santa Cruz, the University of Cambridge, Centro de Investigaciones Energéticas, Medioambientales y Tecnológicas-Madrid, the University of Chicago, University College London, the DES-Brazil Consortium, the University of Edinburgh, the Eidgenössische Technische Hochschule (ETH) Zürich, Fermi National Accelerator Laboratory, the University of Illinois at Urbana-Champaign, the Institut de Ciències de l'Espai (IEEC/CSIC), the Institut de Física d'Altes Energies, Lawrence Berkeley National Laboratory, the Ludwig-Maximilians Universität München and the associated Excellence Cluster Universe, the University of Michigan, the National Optical Astronomy Observatory, the University of Nottingham, The Ohio State University, the University of Pennsylvania, the University of Portsmouth, SLAC National Accelerator Laboratory, Stanford University, the University of Sussex, Texas A&M University, and the OzDES Membership Consortium.

Based in part on observations at Cerro Tololo Inter-American Observatory, National Optical Astronomy Observatory, which is operated by the Association of Universities for Research in Astronomy (AURA) under a cooperative agreement with the National Science Foundation.

The DES data management system is supported by the National Science Foundation under Grant Numbers AST-1138766 and AST-1536171. The DES participants from Spanish institutions are partially supported by MINECO under grants AYA2015-71825, ESP2015-66861, FPA2015-68048, SEV-2016-0588, SEV-2016-0597, and MDM-2015-

0509, some of which include ERDF funds from the European Union. IFAE is partially funded by the CERCA program of the Generalitat de Catalunya. Research leading to these results has received funding from the European Research Council under the European Union's Seventh Framework Program (FP7/2007-2013) including ERC grant agreements 240672, 291329, and 306478. We acknowledge support from the Australian Research Council Centre of Excellence for All-sky Astrophysics (CAASTRO), through project number CE110001020, and the Brazilian Instituto Nacional de Ciência e Tecnologia (INCT) e-Universe (CNPq grant 465376/2014-2).

This manuscript has been authored by Fermi Research Alliance, LLC under Contract No. DE-AC02-07CH11359 with the U.S. Department of Energy, Office of Science, Office of High Energy Physics. The United States Government retains and the publisher, by accepting the article for publication, acknowledges that the United States Government retains a non-exclusive, paid-up, irrevocable, world-wide license to publish or reproduce the published form of this manuscript, or allow others to do so, for United States Government purposes.

We are grateful for the extraordinary contributions of our CTIO colleagues and the DECam Construction, Commissioning and Science Verification teams in achieving the excellent instrument and telescope conditions that have made this work possible. The success of this project also relies critically on the expertise and dedication of the DES Data Management group.

REFERENCES

Ade P. A. R., et al., 2014, Astron. Astrophys., 571, A16
Amiaux J., Scaramella R., Mellier 2012, in Space Telescopes and Instrumentation 2012: Optical, Infrared, and Millimeter Wave Vol. 8442 of Proc. SPIE, Euclid mission: building of a reference survey. p. 84420Z
Bardeen J., Bond J., Kaiser N., Szalay A., 1986, Astrophys. J., 304, 15
Bel J., Hoffmann K., Gaztaaga E., 2015, Mon. Not. Roy. Astron. Soc., 453, 259
Benitez N., 2000, Astrophys. J., 536, 571
Bernardeau F., 1994, Astrophys. J., 433, 1
Bernardeau F., 1996, Astron. Astrophys., 312, 11
Bertin E., Arnouts S., 1996, Astronomy and Astrophysics, Supplement, 117, 393
Blanton M., Cen R., Ostriker J. P., Strauss M. A., Tegmark M., 2000, Astrophys. J., 531, 1
Bouchet F. R., Juszkiewicz R., Colombi S., Pellat R., 1992, Astrophys. J., 394, L5
Carrasco Kind M., Brunner R. J., 2013, Mon. Not. Roy. Astron. Soc., 432, 1483
Carrasco Kind M., Brunner R. J., 2013, MNRAS, 432, 1483
Chang C., Pujol A., Gaztañaga E., Amara A., Réfrégier A., Bacon D., et al., 2016, MNRAS, 459, 3203
Clerkin L., et al., 2016, Mon. Not. Roy. Astron. Soc.
Crocce M., Carretero J., Bauer A. H., Ross A. J., Sevilla-Noarbe I., Giannantonio T., Sobreira F., Sanchez J., Gaztañaga E., DES Collaboration 2016, MNRAS, 455, 4301
Crocce M., Castander F. J., Gaztañaga E., Fosalba P., Carretero J., 2015, Mon. Not. Roy. Astron. Soc., 453, 1513
Crocce M., Fosalba P., Castander F. J., Gaztañaga E., 2010, MNRAS, 403, 1353
Dark Energy Survey Collaboration et al., 2016, MNRAS, 460, 1270
Davis M., Geller M. J., Huchra J., 1978, Astrophys. J., 221, 1
Dressler A., 1980, Astrophys. J., 236, 351
Drlica-Wagner A., et al., 2018, ApJS, 235, 33
Efron B., 1979, The Annals of Statistics, 7, 1
Eriksen M., Gaztanaga E., 2015
Foreman-Mackey D., Hogg D. W., Lang D., Goodman J., 2013, PASP, 125, 306
Fosalba P., Gaztañaga E., Castander F. J., Manera M., 2008, MNRAS, 391, 435
Frieman J. A., Gaztañaga E., 1999, Astrophys. J., 521, L83
Fry J. N., 1996, The Astrophysical Journal Letters, 461, L65
Fry J. N., Gaztañaga E., 1993, Astrophys. J., 413, 447
Garcia-Fernandez M., Sanchez E., Sevilla-Noarbe I., Suchyta E., Huff E. M., Gaztanaga E., Aleksić J., Ponce R., Castander F. J., Hoyle B., Abbott T. M. C., Abdalla F. B., et al., 2018, MNRAS, 476, 1071
Gaztañaga E., 1994, Mon. Not. Roy. Astron. Soc., 268, 913
Gaztanaga E., Eriksen M., Crocce M., Castander F., Fosalba P., et al., 2011
Giannantonio T., Fosalba P., Cawthon R., Omori Y., et al. 2016, MNRAS, 456, 3213
Gil-Marín H., Norea J., Verde L., Percival W. J., Wagner C., Manera M., Schneider D. P., 2015, Mon. Not. Roy. Astron. Soc., 451, 539
Górski K. M., Hivon E., Banday A. J., Wandelt B. D., Hansen F. K., Reinecke M., Bartelmann M., 2005, ApJ, 622, 759
Gruen D., Friedrich O., Krause E., DeRose J., Cawthon R., Davis C., Elvin-Poole J., Rykoff E. S., et al., 2017, ArXiv e-prints
Heath D. J., 1977, MNRAS, 179, 351
Hoffmann K., Bel J., Gaztanaga E., 2015, Mon. Not. Roy. Astron. Soc., 450, 1674
Ivezić Ž., Connolly A., Vanderplas J., Gray A., 2014, Statistics, Data Mining and Machine Learning in Astronomy. Princeton University Press
Ivezić Ž., Kahn S. M., Tyson J. A., Abel B., Acosta E., Allsman R., Alonso D., AlSayyad Y., Anderson S. F., Andrew J., et al. 2008, ArXiv e-prints
Kaiser N., 1984, Astrophys. J., 284, L9
Kollmeier J. A., Zasowski G., Rix 2017, ArXiv e-prints
Leistedt B., Peiris H., Elsner F., Benoit-Levy A., Amara A., et al., 2016, The Astrophysical Journal Suplement, 226, 24
Manera M., Gaztañaga E., 2011, Mon. Not. Roy. Astron. Soc., 415, 383
Manera M., Sheth R. K., Scoccimarro R., 2010, Mon. Not. Roy. Astron. Soc., 402, 589
Mo H. J., White S. D. M., 1996, Mon. Not. Roy. Astron. Soc., 282, 347
Monet D., Levine S., Canzian B., Ables H., Bird A., Dahn C., Guetter H., Harris H., et al., 2003, The Astrophysical Journal, 125, 984
Norberg P., Baugh C., Hawkins E., Maddox S., 2002, Mon.

Not. Roy. Astron. Soc., 332, 827
Norberg P., Baugh C. M., Gaztañaga E., Croton D. J., 2009, MNRAS, 396, 19
Nusser A., Davis M., 1994, Astrophys. J., 421, L1
Peebles P. J. E., 1980, The large-scale structure of the universe. Princeton University Press
Pen U.-L., 1998, The Astrophysical Journal, 504, 601
Pollack J. E., Smith R. E., Porciani C., 2014, Mon. Not. Roy. Astron. Soc., 440, 555
Prat J., Sánchez C., Miquel R., Kwan J., Blazek J., Bonnett C., Amara A., Bridle S. L., Clampitt J., Crocce M., Fosalba P., Gaztanaga E., et al., 2018, MNRAS, 473, 1667
Press W. H., Schechter P., 1974, Astrophys. J., 187, 425
Pujol A., Hoffmann K., Jimnez N., Gaztaaga E., 2017, Astron. Astrophys., 598, A103
Ross A. J., Brunner R. J., Myers A. D., 2006, Astrophys. J., 649, 48
Rozo E., Rykoff E. S., Abate A., Bonnett C., Crocce M., Davis C., Hoyle B., Leistedt B., Peiris H. V., Wechsler R. H., Abbott T., Abdalla F. B., Banerji M., et al., 2016, MNRAS, 461, 1431
Sánchez E., Carnero A., García-Bellido J., Gaztañaga E., de Simoni F., Crocce M., Cabré A., Fosalba P., Alonso D., 2011, MNRAS, 411, 277
Sato M., Matsubara T., 2013, Physical Review Letters D, 87, 123523
Scherrer R. J., Weinberg D. H., 1998, Astrophys. J., 504, 607
Schlegel D., Finkbeiner D., Davis M., 1998, The Astrophysical Journal, 500, 525
Sheth R. K., Tormen G., 1999, Mon. Not. Roy. Astron. Soc., 308, 119
Tegmark M., Peebles P. J. E., 1998, Astrophys. J., 500, L79
Willmer C. N. A., Maia M. A. G., Mendes S. O., Alonso M. V., Rios L. A., Chaves O. L., de Mello D. F., 1999, Astron. J., 118, 1131
Wolk M., McCracken H. J., Colombi S., Fry J. N., Kilbinger M., Hudelot P., Mellier Y., Ilbert O., 2013, MNRAS, 435, 2
Zehavi I., Blanton M., Frieman J., Weinberg D., 2002, Astrophys. J., 571, 172